Volume 14
Number 25
28 April 2026
Pages 15487–16230

Journal of Materials Chemistry A

Materials for energy and sustainability

rsc.li/materials-a

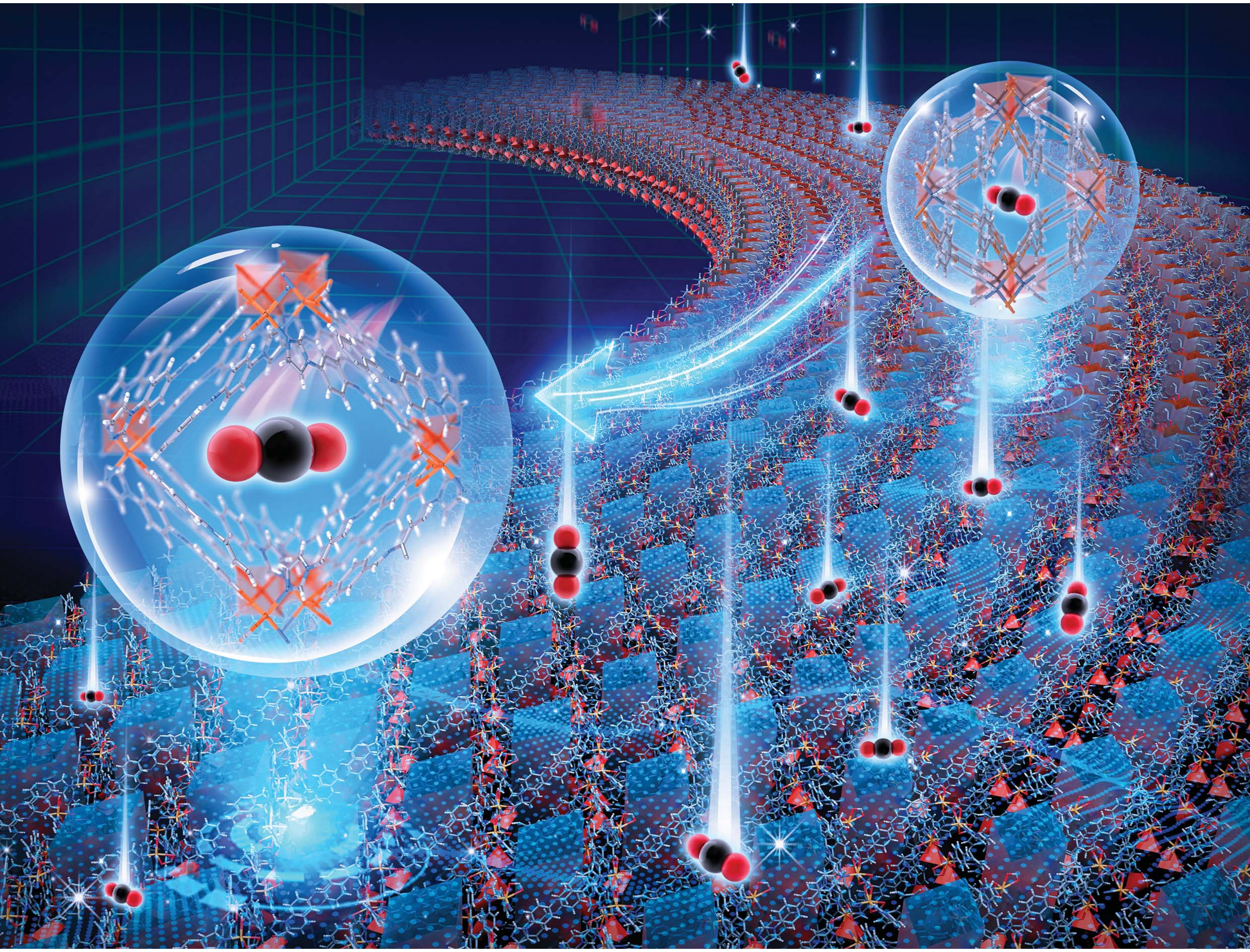

ISSN 2050-7488

ROYAL SOCIETY OF CHEMISTRY

PAPER

Rui Zheng *et al.*

CO_2 adsorption-induced anisotropic mechanical response in an 8-fold interpenetrated diamondoid metal–organic framework

Journal of
Materials Chemistry A

PAPER

View Article Online
View Journal | View Issue

Check for updates

Cite this: *J. Mater. Chem. A*, 2026, **14**, 15721

CO$_2$ adsorption-induced anisotropic mechanical response in an 8-fold interpenetrated diamondoid metal–organic framework

Rui Zheng, Saad Aldin Mohamed, Quan Liu, Xiaoyu Wu * and Jianwen Jiang *

Received 24th February 2026
Accepted 29th March 2026

DOI: 10.1039/d6ta01626j

rsc.li/materials-a

Adsorption in nanoporous adsorbent materials is considered a viable technology for CO$_2$ capture. With intrinsic structural transition and tunable working capacity, flexible metal–organic frameworks (MOFs) hold great potential for energy-efficient CO$_2$ capture. Transitioning MOFs from laboratory-scale to practical capture requires in-depth understanding of their structural behavior and adsorption performance. Nevertheless, interpreting the fundamental mechanism underlying their flexibility from a molecular level poses a significant challenge. Herein, we employ hybrid Monte Carlo/molecular dynamics simulations to explore CO$_2$-induced structural transition of a flexible MOF (X-dia-2-Cd). Stepped isotherms are predicted at different response pressures during CO$_2$ adsorption, which agree well with experiments at both 195 K and 273 K. Structural transition from a narrow pore (Np) phase to a large pore (Lp) phase is observed and revealed to be driven primarily by the deformation of Cd metal nodes. CO$_2$ diffusion is substantially accelerated upon the structural transition from the Np to Lp phase. Moreover, the mechanical strength of X-dia-2-Cd is found to be preserved during the structural transition. From this study, we provide quantitative understanding in the flexibility of X-dia-2-Cd and unravel the microscopic mechanism underlying CO$_2$-induced structural transition by linking its local elastic behavior to multiphase stability. These microscopic insights offer valuable guidance for the rational design of new flexible MOFs for CO$_2$ capture and other industrially important gas adsorption processes.

1 Introduction

Gas adsorption in nanoporous materials has attracted considerable attention due to its potential to address persistent challenges across various industrial applications including energy,[1–3] environment,[4,5] and healthcare fields.[6] In the context of clean energy, there is an increasing drive to reduce CO$_2$ emissions from energy production.[7,8] Metal–organic frameworks (MOFs), characterized by their highly diverse topologies and easily tunable pore sizes, have attracted considerable interest and exhibit superior performance in gas storage and separation.[9–11] A subset of these materials, flexible MOFs, features dynamic frameworks that can change structures and properties in response to external stimuli.[12–16]

While there were a large number of studies on gas adsorption in flexible MOFs, very few investigated how their mechanical strength varies during adsorption process. Typically, the stiffness of a porous material is enhanced upon adsorption. For instance, through molecular dynamics (MD) simulations, Ortiz *et al.*[17] revealed that the presence of CH$_4$ in ZIF-8 significantly increased the mechanical stability of framework. In contrast, flexible MOFs usually exhibit greater stiffness in a guest-free contracted phase compared to a guest-loaded expanded phase due to complex framework rearrangements and sophisticated intermolecular interactions. Neimark *et al.*[18] employed mercury intrusion experiments and demonstrated that compressing MIL-53(Cr) into a narrow pore phase caused a fivefold increase in its bulk modulus from about 2 to 10 GPa. This finding was further corroborated by molecular simulations on MIL-53(Cr).[19] Generally, the mechanical stability of guest-loaded flexible MOFs during phase transition remains elusive. Such transition can be viewed as a mechanical response of framework to stress imposed by guest molecules.[20] Recent experiments demonstrated that the shaped pellets of flexible MIL-53(Al)-OH and MIL-53(Al)-OH$_2$ could not withstand the mechanical stress associated with phase transitions during gas adsorption–desorption cycles, leading to disintegration upon exposure to high-pressure CH$_4$ adsorption.[21] Consequently, understanding the influence of gas adsorption on the stiffness of flexible MOFs is indispensable for determining their mechanical stability or failure.

To precisely describe the mechanical response of flexible MOFs upon gas adsorption, accurate and reliable

---

Department of Chemical and Biomolecular Engineering, National University of Singapore, 117576, Singapore. E-mail: xiaoyu96@nus.edu.sg; chejj@nus.edu.sg

representation of structural transition is essential; nevertheless, modeling such transition is technically challenging. In recent years, several computational approaches have emerged to investigate guest-induced structural transition in flexible MOFs. Ghoufi *et al.* employed a hybrid osmotic Monte Carlo (HOMC) scheme to monitor CO_2-induced transition among discrete phases (Cp, Np and Lp) of MIL-53(Cr).[22] Agrawal and Sholl introduced a flexible snapshot approach to assess adsorption in a series of MD-generated frameworks by neglecting potential guest-induced structural transition.[23] Building on this idea, Rogge *et al.* coupled MC and MD (MC/MD) simulations in an osmotic ensemble to capture the structural transition of MIL-53(Al), allowing for shape variations at a fixed volume.[24] However, these above approaches require prior knowledge of the flexible behavior of a MOF and rely on experimentally available structures along the transition pathway. More generally, simulations can be carried out starting from a single discretized structure of a MOF. We precisely captured N_2-induced structural transition of ZIF-8 using the hybrid Gibbs-ensemble MC/MD (GEMC/MD) method[25] and further examined the adsorption of C_1–C_4 alcohols in ZIF-8 through the hybrid grand-canonical MC/MD (GCMC/MD) method.[26] Yu *et al.* applied the hybrid GCMC/MD method to examine CO_2-induced breathing behavior starting from the Lp phase of MIL-53.[27] More recently, we developed a systematic approach to incorporate structural flexibility into high-throughput computational screening of MOFs for xylene separation.[28] With this method, we also quantitatively evaluated the structural transition induced by C_4 alkanes and olefins in flexible Flex-Cd-MOF-2a.[29] Apparently, accurate force fields (FFs) are essential to reliable simulations of structural transition during adsorption in flexible MOFs. A handful of FFs such as MOF-FF[30] have been shown to accurately reproduce the experimental structures and adsorption behavior of certain flexible MOFs; however, they are typically tailored to specific MOFs and possess limited transferability. General FFs, including the universal FF (UFF)[31] and UFF4MOF,[32,33] are more broadly applicable but require careful validation, particularly for flexible MOFs where significant structural deformation occurs.

Although adsorption-induced stress has been studied as a trigger for phase transition in MIL-53(Al),[34] the evolution of mechanical strength in guest-loaded frameworks during phase transition remains largely unexplored. Fundamental understanding of how guests influence mechanical strength is particularly intriguing and relevant during the processing and shaping of flexible MOFs in industrial applications. In this study, we investigate CO_2-induced continuous transition from a narrow pore (Np) phase to a large pore (Lp) phase in a flexible MOF, namely X-dia-2-Cd (Fig. 1a–c).[12] Fig. 1d illustrates the Cd-centered tetrahedral building block that assembles into an interpenetrated adamantoid cage in X-dia-2-Cd. In addition to quantitatively reproducing experimental CO_2 adsorption isotherms at 195 and 273 K, we also predict the evolution of mechanical strength induced by CO_2 adsorption (Fig. 1e). While this work is focused on a specific MOF, the microscopic insights could be generalized to other flexible MOFs, thereby supporting the anticipation of similar structural responses to various adsorbates.

2 Methodology

2.1. Force fields

Fig. S1 illustrates the atomic types of X-dia-2-Cd. The intra-framework interactions were mimicked by bonded and non-bonded potentials. The bonded potential comprised bond stretching and bending and proper and improper torsional terms:

$$U_{\text{bonded}} = U_{\text{stretching}} + U_{\text{bending}} + U_{\text{proper}} + U_{\text{improper}} \tag{1}$$

$$U_{\text{stretching}} = \sum k_{\text{b}}(r - r_0)^2 \tag{2}$$

$$U_{\text{bending}} = \sum \frac{k_\theta}{n^2}[1 - B(-1)^n\cos(n\theta)] \tag{3}$$

$$U_{\text{bending}} = \sum k_\theta[C_0^{\text{bend}} + C_1^{\text{bend}}\cos(\theta) + C_2^{\text{bend}}\cos(2\theta)] \tag{4}$$

$$U_{\text{proper}} = \sum k_\phi[1 + d\cos(n\phi)] \tag{5}$$

$$U_{\text{improper}} = \sum k_\xi[C_0^{\text{imp}} + C_1^{\text{imp}}\cos(\xi) + C_2^{\text{imp}}\cos(2\xi)] \tag{6}$$

where k_{b}, k_θ, k_ϕ, and k_ξ are the force constants, r, θ, ϕ, and ξ are bond lengths, bond angles, proper and improper torsional angles, r_0 is the equilibrium value, B and d are the phase factors and were set -1 or 1, n refers to periodicity, and C_i^{bend} and C_i^{imp} are dimensionless coefficients defining the angle bending and improper torsional potentials, respectively. The potential parameters were derived from UFF4MOF,[32,33] as listed in Tables S1–S6. The non-bonded potential included Lennard–Jones (LJ) and coulombic terms:

$$U_{\text{non-bonded}} = U_{\text{LJ}} + U_{\text{coulombic}} \tag{7}$$

$$U_{\text{LJ}} = \sum 4\varepsilon_{ij}\left[\left(\frac{\sigma_{ij}}{r_{ij}}\right)^{12} - \left(\frac{\sigma_{ij}}{r_{ij}}\right)^{6}\right] \tag{8}$$

$$U_{\text{coulombic}} = \sum \frac{q_i q_j}{4\pi\varepsilon_0 r_{ij}} \tag{9}$$

where ε_{ij} is the well depth, σ_{ij} is the collision diameter, and r_{ij} is the distance between two atoms. q_i and q_j are the atomic charges, and ε_0 is the dielectric constant. CO_2 molecule was represented using the transferable potentials for phase equilibria-united atoms (TRAPPE-UA).[35] In simulation studies of gas adsorption in MOFs, the atomic charges of frameworks are usually evaluated from DFT-trained machine-learning models, as implemented in PACMOF,[36] PACMAN,[37] and MEPO-ML.[38] We attempted to simulate CO_2 adsorption isotherms in X-dia-2-Cd at 273 K using various charge methods. Fig. S2a shows that PACMOF captures the CO_2-induced structural transition of X-dia-2-Cd well and gives the best agreement with the available experimental isotherms. Consequently, PACMOF was used to derive the atomic charges of X-dia-2-Cd. With the PACMOF charge method, we further compared the isotherms using various FFs. As demonstrated in Fig. S2b,

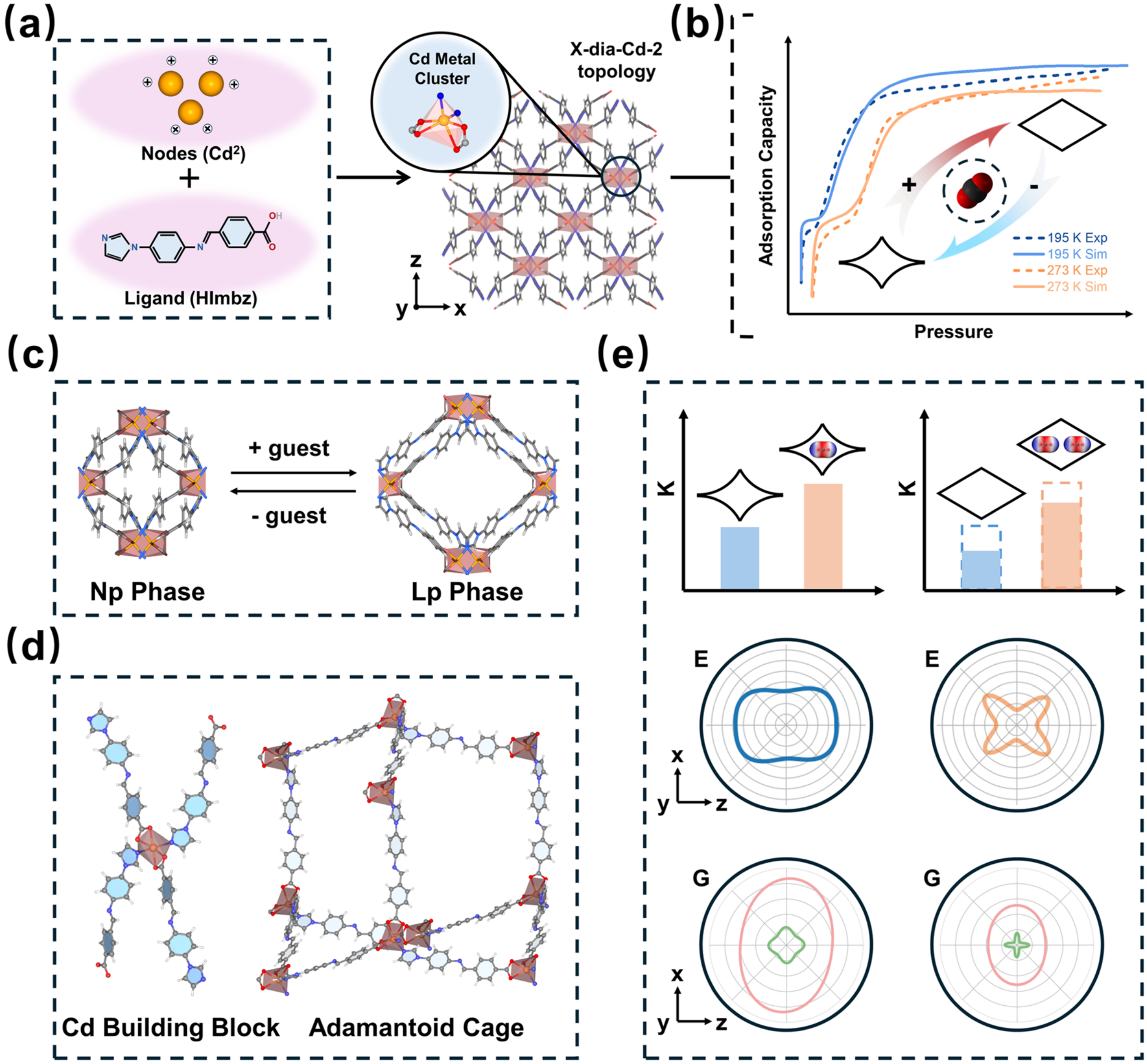

Fig. 1 (a) Cd^{2+} metal node, 4-((4-(1H-imidazole-1-yl)phenylimino)methyl)benzoic acid (HImbz) linker, and topology of X-dia-2-Cd. (b) CO_2 adsorption isotherms at 195 K and 273 K. (c) Schematic of guest-induced phase transition in X-dia-2-Cd. (d) Cd-centered tetrahedral building block and an adamantoid cage. (e) Mechanical properties of CO_2-loaded X-dia-2-Cd in Np and Lp phases, respectively.

UFF4MOF[32,33] outperforms UFF-fix-metal[39] and Dreiding[40] in predicting CO_2 adsorption in X-dia-2-Cd. Among the three FFs, UFF4MOF is the only one that correctly predicts the structural transition of X-dia-2-Cd and it also accurately predicts CO_2 uptakes over a very wide pressure range from 0 to 30 bar. The FFs adopted (PACMOF + UFF4MOF) are expected to be also applicable across a wide temperature range, providing insights into CO_2 adsorption behavior where experimental data are lacking.

2.2. Simulation methods

Based on the above FFs, we first relaxed the structure of X-dia-2-Cd using a supercell (2 × 2 × 2 unit cells) of the Np phase. This FF-relaxation was performed *via* conjugate gradient energy minimization in the LAMMPS package,[41] with the supercell shape and volume allowed to vary. To validate the relaxed structure, DFT calculations were conducted using the PADE exchange–correlation functional with the BFGS algorithm, as implemented in the CP2K package.[42] All the atoms except Cd were treated using the GPW method with the TZVP basis set and GTH pseudo-potentials, while the DZVP-SR basis set was used for Cd atom. The plane wave cutoff for electron density was set to 400 Ry.

The FF-relaxed structure was used to simulate CO_2 adsorption in X-dia-2-Cd. To account for framework flexibility, the hybrid GCMC/MD method was adopted. In this protocol, GCMC simulations were first performed in the Np phase at a given pressure; thereafter, MD simulations were carried out to allow structural variation. The iterative GCMC/MD loops were conducted using a revised TAXI interface[27] as in our previous work.[28,29] The iteration was repeated for a minimum of 10 loops before convergence was achieved (Fig. S3 and S4). The Gelman–

Rubin diagnostic factor (R-factor)[43,44] was adopted to determine convergence, defined as:

$$R = \frac{m+1}{m}\frac{B}{W} + \frac{n-1}{n} \tag{10}$$

where m is the number of iterations used for convergence assessment, set to four in this study, n is the number of sampling cycles per iteration, B corresponds to the variance among the means of the m iterations, and W is the average of variances within each iteration. Given the large n used in the GCMC simulation, the second term in the formula tends to be equal to one. An R-factor near one signals convergence, while a greater value indicates that additional sampling is needed. In this work, an R-factor threshold of 1.5 (Fig. S5 and S6) was adopted as the convergence criterion for CO_2 adsorption, which is commonly used as a threshold in hybrid GCMC/MD simulations.[28,29,45–48] Concurrently, the evolution of lattice parameters was tracked during the simulation (Fig. S7–S10). While the supercell lattice parameters were found to stabilize upon reaching convergence, a more accurate determination would require the R-factor.

In the hybrid GCMC/MD protocol, GCMC simulations were performed in the RASPA package.[49] For CO_2 adsorption at 195 K and 273 K, each GCMC simulation included 20 000 cycles, equally divided into equilibration and production. Four types of trial moves including translation, rotation, reinsertion and swap were conducted. MD simulations were carried out in the LAMMPS package[41] for the CO_2-loaded structure. Each MD simulation lasted for 0.2 ns, with 0.1 ns in a canonical (*NVT*) ensemble and 0.1 ns in an isothermal isobaric (*NPT*) ensemble. Temperature and pressure were regulated *via* a thermostat and barostat with a 0.1 ps coupling constant. A time step of 1 fs was used for integrating the equations of motion. Periodic boundary conditions were applied in all three directions. The LJ interactions were calculated using a spherical cutoff of 12.8 Å, with the cross LJ interactions evaluated by the Lorentz–Berthelot mixing rules. The coulombic interactions were treated using Ewald summation, while those between framework atoms were excluded.[39,50] The hybrid GCMC/MD iterations allowed X-dia-2-Cd structure to vary during CO_2 adsorption. As CO_2 loading increased (*i.e.*, at a high pressure of CO_2), structural transition from the Np to Lp phase was observed (Fig. 1b and c). CO_2 adsorption isotherms at 195 K and 273 K were simulated, starting from the Np phase over pressure ranges of 0.001 to 1.0 bar and to 30 bar, respectively. At each pressure, adsorption capacity was averaged over five independent runs and reported using the excess amount to ensure direct comparison with experimental data.

2.3. Characterization

To characterize X-dia-2-Cd structure, the distributions of three representative angles (O–Cd–O, N–Cd–N and O–Cd–N) in Cd metal nodes were calculated in both Np and Lp phases. Moreover, the structural profiles of Cd–Cd pairs and CO_2 molecules in X-dia-2-Cd were estimated *via* radial distribution function (RDF):

$$g_{ij}(r) = \frac{N_{ij}(r, r+\Delta r)V}{4\pi r^2 \Delta r N_i N_j} \tag{11}$$

where r is the distance between atoms i and j, $N_{ij}(r, r + \Delta r)$ is the number of atoms j around center atoms i with a spherical cutoff from r to $r + \Delta r$, V is the system volume, and N_i and N_j are the numbers of atoms i and j, respectively. The C atoms of CO_2 molecules were taken as the center. Meanwhile, the dynamics of CO_2 molecules in X-dia-2-Cd was quantified by mean-squared displacement (MSD):

$$\mathrm{MSD}(t) = \frac{1}{N}\sum_{i=1}^{N}\left\langle |r_i(t) - r_i(0)|^2 \right\rangle \tag{12}$$

where N is the number of molecules and $r_i(t)$ is the position of particle i at time t. To improve statistics, the multiple time origin scheme was employed.[51] To calculate angle distributions, RDFs and MSDs, configurations from the last four hybrid GCMC/MD iterations were used. In each configuration, CO_2 molecules were loaded into X-dia-2-Cd, energy minimized using the conjugate gradient method, and followed by MD simulations. The initial 20 ns MD simulation was performed in a microcanonical (*NVE*) ensemble using the Berendsen thermostat to reach equilibrium. Thereafter, a 20 ns MD simulation was conducted in a canonical (*NVT*) ensemble, employing the Nosé–Hoover thermostat with a relaxation time of 0.1 ps. Throughout these simulations, the MOF framework was treated as fully flexible, with all atom positions allowed to change freely.

2.4. Mechanical properties

2.4.1. Explicit deformation method. The bulk moduli of empty and CO_2-loaded X-dia-2-Cd were calculated at 0 K and 0 atm using the explicit deformation method. The initial structures were obtained from the final snapshots of hybrid GCMC/MD simulations at 273 K. In this method, a structure was first optimized *via* two consecutive procedures: (1) a conjugate gradient (CG) algorithm with anisotropic cell relaxation at zero pressure, and (2) the FIRE algorithm under a fixed cell shape and volume. The CG-FIRE loop was repeated five times with a small perturbation introduced between cycles to ensure convergence, using a tolerance of 10^{-15} and a maximum of 10^5 iterations per loop. Subsequently, ±1% strain was applied along each lattice direction, and atomic positions were relaxed by MD simulations. The elastic stiffness tensor was then derived from the stress tensor of deformed structure.[52,53] It is worth noting that the explicit deformation method relies on the generalized Hooke's law and is thus applicable only in the elastic (linear) regime. As shown in Fig. S11, the bulk modulus of CO_2-loaded X-dia-2-Cd is observed to remain nearly identical over a range of small strains, with a relative standard deviation of less than 2%, confirming the validity of the linear elasticity assumption.

2.4.2. Strain-fluctuation method. To analyze the mechanical properties of CO_2-loaded X-dia-2-Cd at finite temperatures, the strain-fluctuation method was employed in a (N, σ, T) ensemble.[54,55] The initial structures were obtained from the final snapshots of hybrid GCMC/MD simulations. In this method, a structure was first equilibrated for 2 ns in a *NPT* (aniso) ensemble, followed by an additional 2 ns equilibration in a *NPT* (tri) ensemble. In the production run, the simulation was performed in a *NPT* (tri) ensemble for 4 ns, during which the cell parameters were collected every 10 fs. At a given temperature and pressure, the simulation was conducted using the Nosé–Hoover thermostat and barostat with a coupling constant of 0.1 ps and 1 ps, respectively. A time step of 1 fs was used. To evaluate mechanical properties, the full elastic stiffness tensor **C** was extracted from the fluctuations of the 2 × 2 × 2 supercell matrix **h** using the following relation:

$$\left(\frac{k_B T}{V}\right)\mathbf{C}_{ijkl}{}^{-1} = \langle \varepsilon_{ij}\varepsilon_{kl}\rangle - \langle \varepsilon_{ij}\rangle\langle \varepsilon_{kl}\rangle \tag{13}$$

where k_B is the Boltzmann constant, $\mathbf{C}_{ijkl}$ represents the components of the fourth-order elastic stiffness tensor C, $\langle\varepsilon\rangle$ refers to the time average of ε, and ε is the strain of the 2 × 2 × 2 supercell defined as follows:

$$\varepsilon = \frac{1}{2}\left(\left(\mathbf{h}_0{}^T\right)^{-1}\mathbf{h}^T\mathbf{h}\mathbf{h}_0{}^{-1} - 1\right) \tag{14}$$

where $\mathbf{h}_0$ is the reference supercell, taken as the time-averaged supercell over the production trajectory. The elastic stiffness tensor was extracted after the convergence of supercell volume (Fig. S12 and S13) and elastic constants (Fig. S14–S17). From the elastic stiffness tensor, key mechanical properties, including bulk moduli *K*, linear compressibility *β*, Young's moduli *E*, and shear moduli *G*, were calculated using the ELATE code.[56] For consistency, all the reported elastic constants were based on the Hill averaging scheme (see Section S4 in the SI).

3 Results and discussion

3.1. Structural properties

Fig. S18 compares DFT-optimized and FF-relaxed structures with the experimental structure of X-dia-2-Cd in the Np phase. The three structures appear rather similar, with lattice constants and volumes summarized in Table S7. Notably, the lattice constants and volume from the FF-relaxed structure are in closer agreement with experimental values than those of the DFT-optimized structure. This confirms that the FF (UFF4MOF) adopted provides a reliable description of X-dia-2-Cd.

3.2. CO_2 adsorption in X-dia-2-Cd

As demonstrated in Fig. S2, the FFs (PACMOF + UFF4MOF) can successfully reproduce the experimentally observed structural transition of X-dia-2-Cd upon CO_2 adsorption and accurately predict CO_2 uptakes at 273 K. Fig. 2 shows CO_2 adsorption isotherms at both 195 and 273 K. Remarkable agreement is observed between simulations and experiments at both temperatures, particularly in reproducing the stepped structural transition from the Np to Lp phase, which manifests as three distinct regions. In Region I (Np phase), CO_2 uptakes increase with pressure from 6.3 to 31.2 cm^3 g^{-1} at 195 K (0.001 bar ≤ P ≤ 0.05 bar) and from 0.1 to 37.5 cm^3 g^{-1} at 273 K (0.001 bar ≤ P ≤ 5 bar). Region II corresponds to the gradual transition from the Np to Lp phase, during which CO_2 uptakes increase from 31.2 to 83.8 cm^3 g^{-1} at 195 K (0.05 ≤ P ≤ 0.2 bar) and from 37.5 to 72.1 cm^3 g^{-1} at 273 K (5 ≤ P ≤ 7.5 bar). Region III (Lp phase) shows nearly saturated CO_2 uptakes, reaching 94.2 cm^3 g^{-1} at 195 K and 87.9 cm^3 g^{-1} at 273 K. Notably, the uptakes at both temperatures in Region I are slightly overestimated by simulations. This can be attributed to the LJ parameters in UFF4MOF, which systematically overpredict CO_2 adsorption at low pressures.[57] In Region II, the simulations qualitatively and quantitatively capture CO_2-induced structural transition from the Np to Lp phase. In Region III, CO_2 uptakes near saturation closely match measured data. These results imply that the hybrid GCMC/MD simulation protocol reliably and accurately predicts CO_2 adsorption in X-dia-2-Cd and associated structural transition at different temperatures and pressures, highlighting its potential extension to broader conditions and other flexible MOFs.

3.3. Structural transition

As noted above, the structural transition from the Np to Lp phase in X-dia-2-Cd occurs when the pressure exceeds a turning point (0.05 bar at 195 K and 5 bar at 273 K, respectively) during CO_2 adsorption. A video illustrating the structural transition is provided in the SI. This transition is driven by the expansion of one-dimensional (1D) channels in X-dia-2-Cd, as well as the motion of CO_2 molecules in the framework. Fig. 3a and d depict the angle distributions of Cd metal nodes in the Np and Lp phase of X-dia-2-Cd. At 195 and 273 K, the intensity of O–Cd–O angle exhibits a similar shift from the Np to Lp phase: increasing at ∼80° and decreasing at ∼113° and ∼160°. For N–Cd–N angle at ∼110°, its intensity decreases. Such changes in O–Cd–O and N–Cd–N angles also cause an increase in the intensity of N–Cd–O angle at ∼130°. These angle distributions indicate that CO_2 adsorption in X-dia-2-Cd leads to similar structures in the Lp phase at both 195 and 273 K. Fig. 3b and e show the RDFs of Cd–Cd metal pairs, revealing that the deformation of Cd metal node during the structural transition causes a slight linker distortion of Cd–Cd distance. Specifically, Cd–Cd distances along the diagonal of the rhombic channels increase from 10.9 to 11.7 Å at 195 K and from 12.0 to 12.6 Å at 273 K, respectively. Fig. 3c and f illustrate the widening of adamantoid cages, manifested by two distinct Cd–Cd–Cd angles. At 195 K, one Cd–Cd–Cd angle decreases from 129.3° to 127.1°, while the other increases from 69.2° to 75.6°. At 273 K, one decreases from 128.8° to 127.0° and the other increases from 69.7° to 74.7°. These findings suggest that local deformation of Cd metal nodes drives the structural transition, further resulting in the widening of adamantoid cages and the expansion of 1D channels, in agreement with experimental observations.[12]

Dynamic motion of CO_2 molecules in X-dia-2-Cd was characterized by MSDs along the channel direction (MSD_y). As shown in Fig. 4a and b, MSDs show similar qualitative trends at both temperatures. In the Np phase, CO_2 molecules display limited mobility, with small MSD values at 195 K and 0.05 bar, as well as 273 K and 2.5 bar. By contrast, a pronounced increase in the MSD is observed upon the structural transition from the Np to Lp phase, occurring when pressure reaches 1.0 bar at 195 K and 30 bar at 273 K, respectively. Fig. 4c presents the cross-

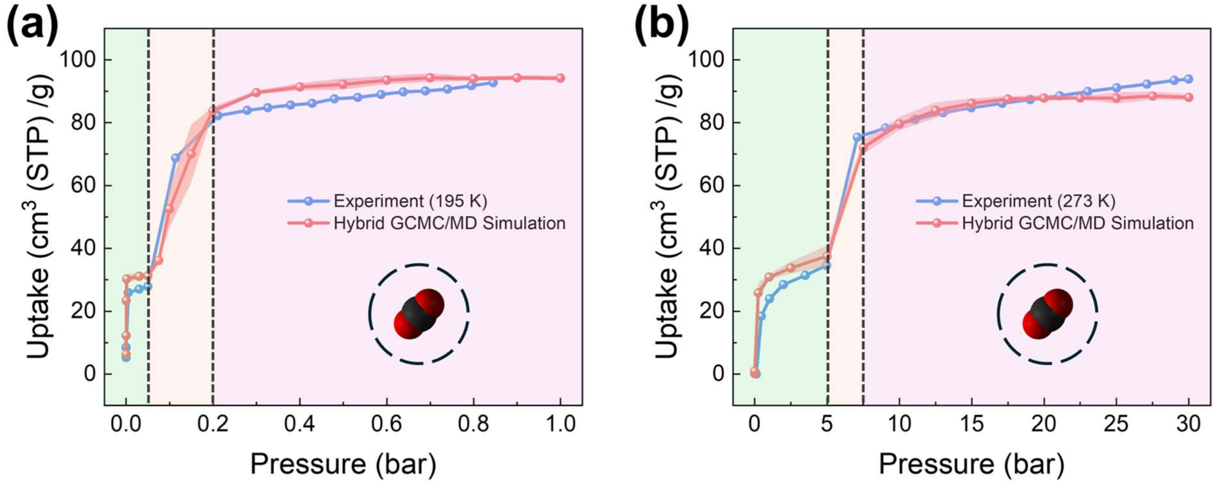

Fig. 2 CO_2 adsorption isotherms in X-dia-2-Cd from hybrid GCMC/MD simulations and experiments[12] at (a) 195 K and (b) 273 K. The shaded areas surrounding the curves represent the standard deviations calculated from five independent simulations at each pressure. Regions I, II, and III are shown in green, yellow and pink, respectively.

sectional views of 1D channels along the *y*-axis at 273 K. A clear enlargement of the channels is directly observed in the Lp phase, indicating the formation of more open pathways for CO_2 diffusion. Fig. 4d compares the channel diameters in the Np and Lp phases at 273 K. In the Np phase, the diameter ranges from 3.3 to 3.9 Å, whereas upon transition to the Lp phase, the diameter increases to between 4.2 Å and 4.8 Å. These results indicate that the markedly larger MSDs in the Lp phase originate from the expanded 1D channels, which provide larger internal free volume for CO_2 diffusion. Furthermore, the greater

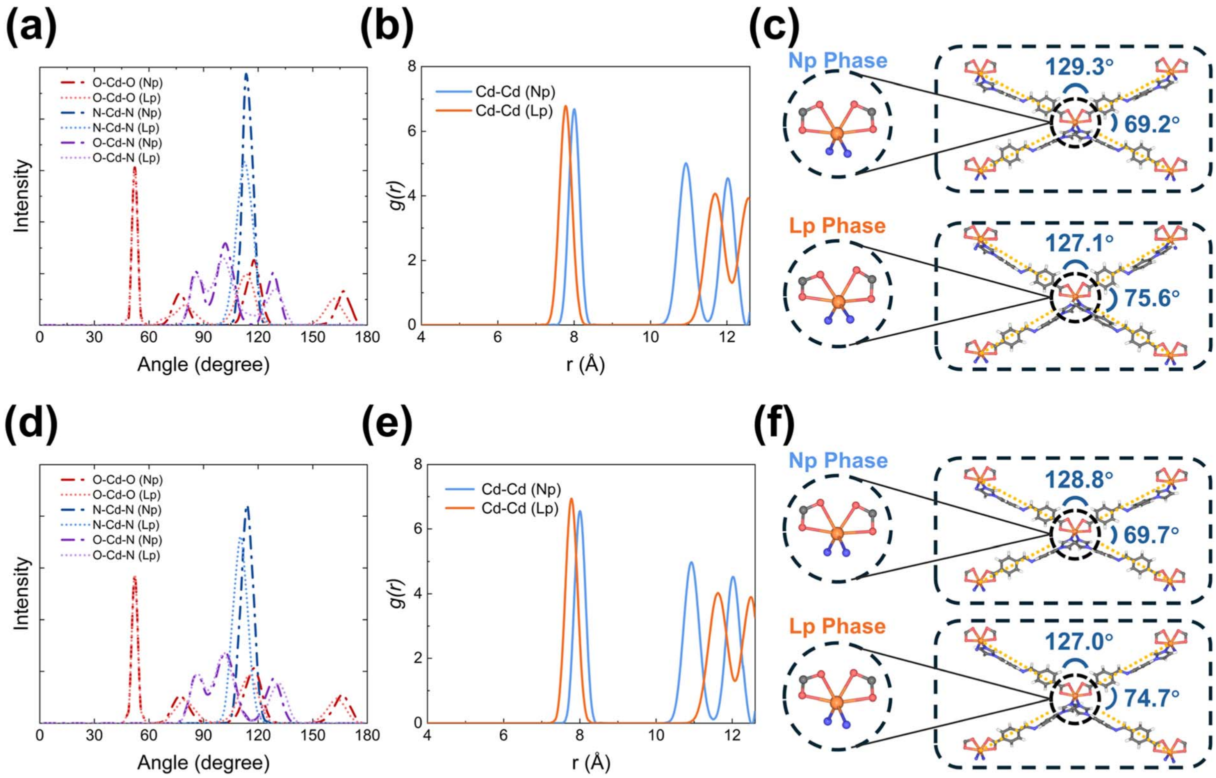

Fig. 3 (a) Angle distributions of Cd metal nodes, (b) RDFs of Cd–Cd pairs, and (c) comparison of the Cd network (Cd–Cd–Cd angle) at 195 K in Np (0.05 bar) and Lp (1.0 bar) phases of X-dia-2-Cd. (d) Angle distributions of Cd metal nodes, (e) RDFs of Cd–Cd pairs, and (f) comparison of the Cd network (Cd–Cd–Cd angle) at 273 K in Np (2.5 bar) and Lp (30 bar) phases of X-dia-2-Cd. The Cd–Cd–Cd angles shown in (c and f) correspond to 3D angles in space.

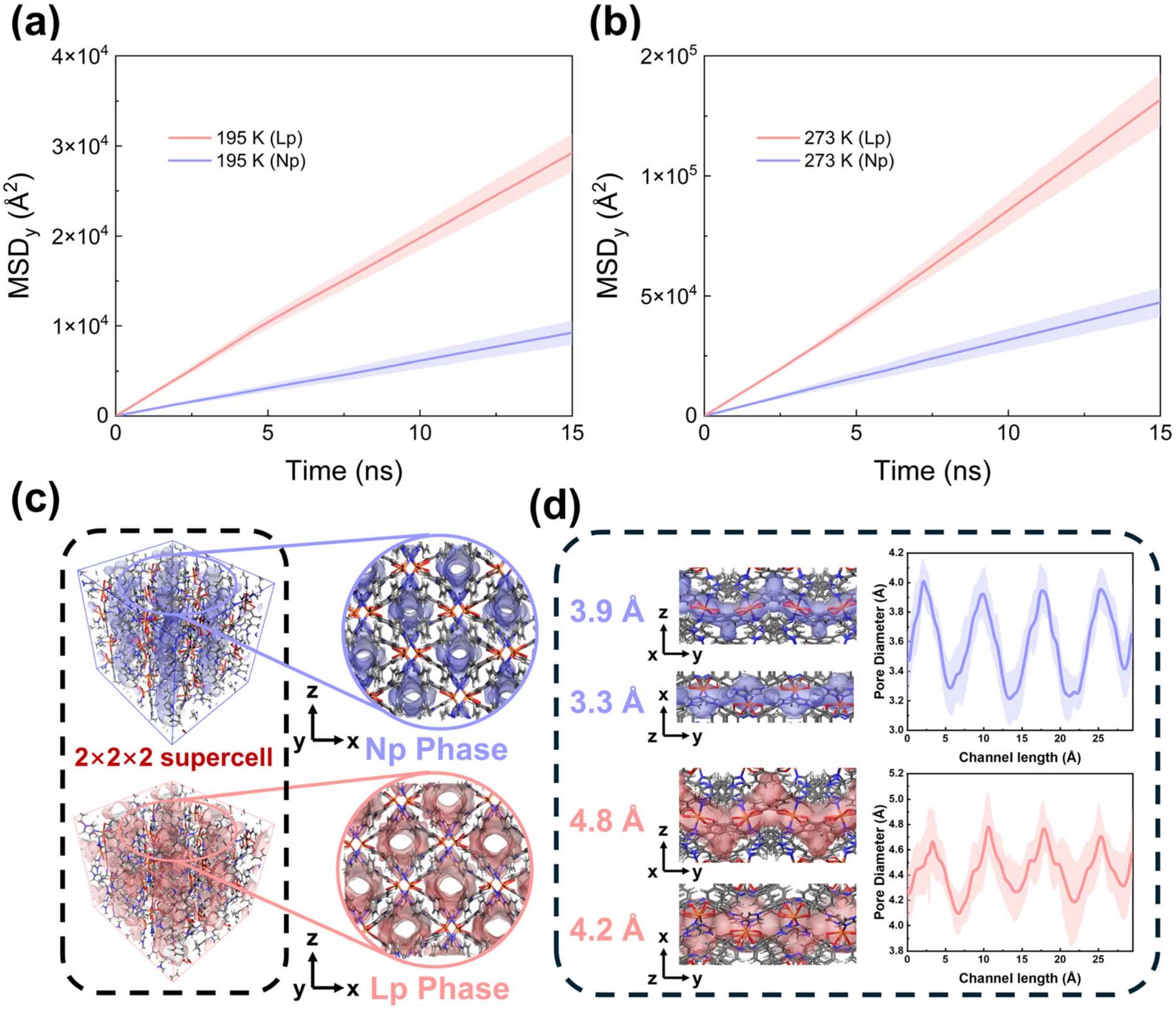

Fig. 4 (a) MSDs of CO_2 at 195 K in Np (0.05 bar) and Lp (1.0 bar) phases. (b) MSDs of CO_2 at 273 K in Np (2.5 bar) and Lp (30 bar) phases of X-dia-2-Cd. The shaded region denotes standard deviation calculated from the last four hybrid GCMC/MD loops. (c) Cross-sectional view of 1D channels along the channel direction (*y* axis). (d) Cross-sectional views of 1D channels along the *x* and *z* axes, together with the channel diameters, in Np and Lp phases. The shaded region denotes the standard deviation for all 1D channels in the supercell, based on the last snapshot from hybrid GCMC/MD simulations (273 K, Np: 2.5 bar, Lp: 30 bar, CO_2 molecules removed).

MSD observed at 273 K can be attributed to the enhanced thermal motion of CO_2 molecules.

To elucidate the interactions between CO_2 molecules and framework, RDFs were calculated. Fig. 5a and b present the RDFs of CO_2 around Cd, N_1, and N_2 atoms of X-dia-2-Cd at 273 K. In the Np phase (2.5 bar), pronounced and concentrated peaks are observed for CO_2 around all three framework atoms. For Cd-(CO_2) pair, distinct peaks appear at ~4.1 and 7.1 Å. The RDF of N_1-(CO_2) exhibits a primary peak at ~4.8 Å and a secondary peak at ~8.7 Å, while the RDF of N_2-(CO_2) shows two notable peaks near 7.2 and 10.5 Å. These peaks reflect the geometric confinement imposed by the narrow 1D channels in the Np phase, resulting in a high degree of structural order and well-defined CO_2-framework interaction distances. Upon transition from the Np to Lp phase, these RDF peaks become broader and reduce in intensity. This reflects a redistribution of CO_2 molecules in the expanded channels and a weaker localization of CO_2 around specific framework atoms, which is consistent with the increased configurational freedom in the Lp phase. Notably, the persistence of the first peaks around Cd, N_1 and N_2 atoms suggests that these atoms remain relevant to CO_2-framework interactions after structural transition, although their interaction strength is attenuated. Fig. 5c and d show the atomic types of X-dia-2-Cd and visualizes CO_2 adsorption in the 1D channel at 2.5 bar in the Np phase and at 30 bar in the Lp phase, respectively. In the Np phase, CO_2 molecules are confined to localized adsorption sites, consistent with the sharp RDF peaks in Fig. 5a. Upon transition from the Np to Lp phase, the expansion of 1D channels enables CO_2 molecules to access a larger volume, resulting in a more delocalized pattern and broader RDF peaks (Fig. 5b). Meanwhile, this delocalization is accompanied by the formation of additional adsorption sites and the rearrangement of CO_2 molecules, in agreement with the RDF results.

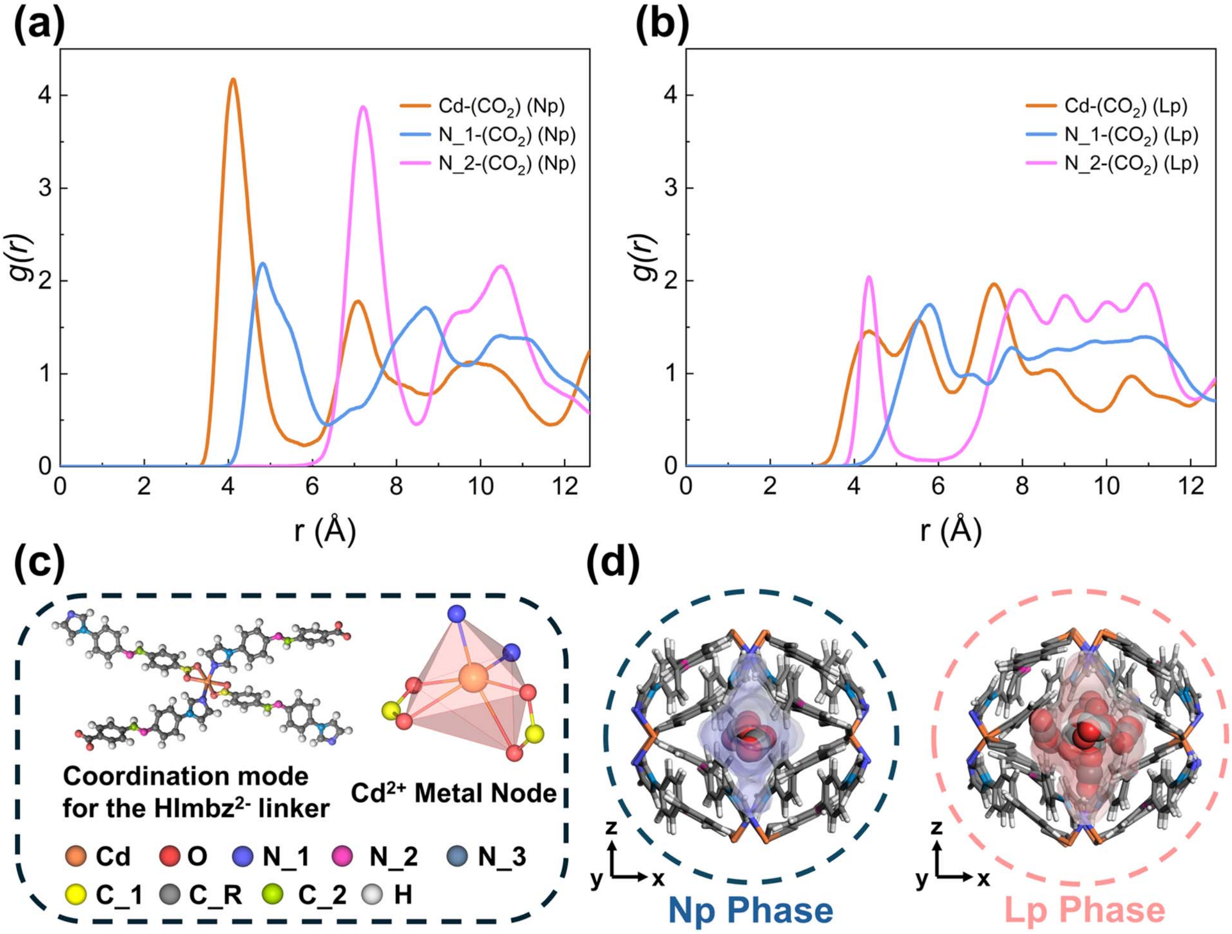

Fig. 5 RDFs for CO_2 around Cd, N_1, and N_2 atoms of X-dia-2-Cd at 273 K. (a) 2.5 bar in the Np phase and (b) 30 bar in the Lp phase. (c) Atomic types of X-dia-2-Cd. (d) Visualization for CO_2 adsorption at 273 K along the *y* axis at 2.5 bar in the Np phase and 30 bar in the Lp phase, respectively.

3.4. Mechanical properties of X-dia-2-Cd

After validating the simulated structural transition and CO_2 adsorption at 195 and 273 K, the key mechanical properties of X-dia-2-Cd during CO_2 adsorption were predicted. Fig. 6a displays three representative mechanical properties: bulk modulus (K), Young's modulus (E) and shear modulus (G). K is the isotropic measure of resistance to volumetric deformation under stress and correlates with fracture resistance. As shown in Fig. 6b, the bulk moduli (K_T) of X-dia-2-Cd at both 195 and 273 K exhibit characteristic stepped variations with CO_2 pressure. Specifically, in the Np phase, K_T increases from 11.9 to 12.6 GPa at 195 K and from 10.8 to 12.1 GPa at 273 K. Upon structural transition, K_T undergoes a drop, decreasing from 12.6 to 12.3 GPa and finally reaching 11.5 GPa at 1.0 bar and 195 K, and from 12.1 to 10.4 GPa, finally reaching 10.1 GPa at 30 bar and 273 K. Notably, the stepwise behavior of K_T shows an opposite trend to that of the stepped CO_2 adsorption isotherm, although the turning points coincide. This reflects the combined effect of framework rearrangement and increase of CO_2 uptake during structural transition. To further elucidate their contributions to framework stiffness, bulk moduli (K_0) of CO_2-loaded and -free frameworks at 0 K and 0 atm were calculated using the explicit deformation method. As shown in Fig. 6c, in the absence of CO_2, K_0 decreases slightly in the Np phase and then drops sharply by about 3.9 GPa upon structural transition. In contrast, CO_2 adsorption markedly enhances the framework stiffness, increasing K_0 by 1.3 GPa in the Np phase and 5.3 GPa in the Lp phase, respectively. K_T and K_0 results indicate that the structural transition intrinsically reduces the stiffness of X-dia-2-Cd, whereas CO_2 adsorption counteracts this effect, leading to only a modest decrease in bulk moduli of CO_2-loaded X-dia-2-Cd during structural transition. Compared to 195 K, K_T at 273 K is reduced due to thermally induced softening.[58,59] Interestingly, in certain porous materials with ample cavities, both experimental and computational studies demonstrated an initial softening effect (*i.e.*, reduced bulk moduli) during adsorption,[60–62] as attributed to adsorption induced internal stresses and the contraction of spacious channels during the initial stage of adsorption. By contrast, no initial softening is observed in X-dia-2-Cd, as the channel size in the Np phase is comparable to the kinetic diameter of CO_2. This observation is consistent with the report by Emelianova *et al.*[63]

Linear compressibility (β_i) along a crystallographic axis defines the directional response to stress, which is related to K

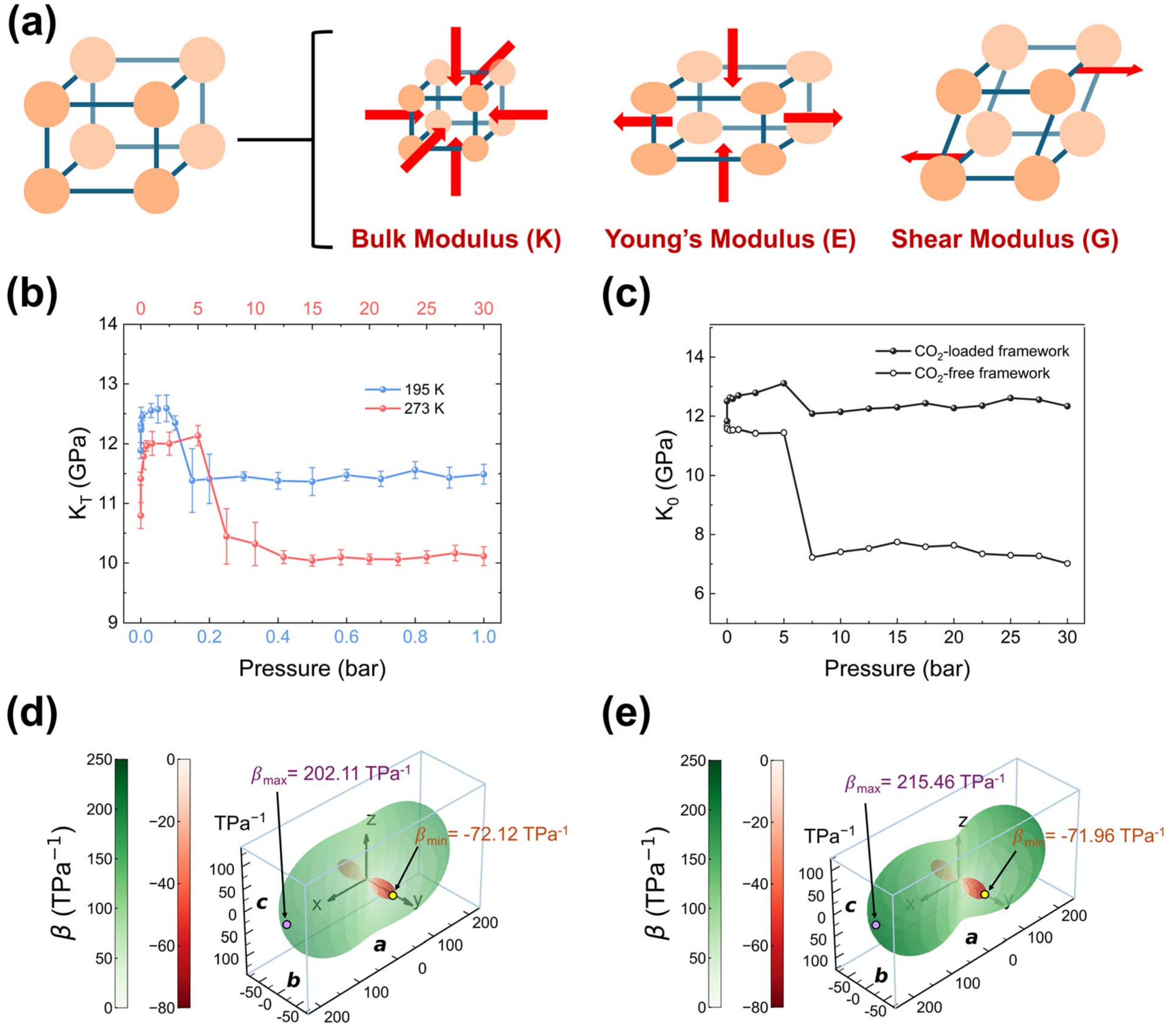

Fig. 6 (a) Three representative elastic properties: bulk modulus (K), Young's modulus (E), and shear modulus (G). (b) Bulk moduli (K_T) of CO_2-loaded X-dia-2-Cd *versus* CO_2 pressure calculated using the strain-fluctuation method at 195 K and 273 K, respectively. The error bars represent the standard deviations from five independent simulations at each pressure. (c) Bulk moduli (K_0) of CO_2-loaded and -free X-dia-2-Cd at 0 K and 0 atm calculated using the explicit deformation method. The initial structure was based on CO_2-loaded X-dia-2-Cd at 273 K from hybrid GCMC/MD simulations. Linear compressibilities (β) at 273 K: (d) 2.5 bar in the Np phase and (e) 30 bar in the Lp phase, shown as a representative sample from one of five independent calculations.

by $K = \dfrac{1}{\beta_a + \beta_b + \beta_c}$. Fig. 6d and e display the anisotropic β of CO_2-loaded X-dia-2-Cd at 273 K. Notably, pronounced negative β (NLC) is observed exclusively along the y axis, reaching a minimum of -72.12 and -71.96 TPa^{-1} in Np and Lp phases, respectively. In contrast, conventional positive β exists along the x and z axes with maximum of 202.11 and 215.46 TPa^{-1} in Np and Lp phases, respectively. NLC manifests as expansion along a single crystallographic axis under pressure, reflecting a high degree of structural anisotropy. It can be attributed to the distortion of adamantoid cages during the structural transition. Fig. S19 shows that the cages undergo hinge-like deformation, whereby angular changes in the diamondoid network lead to the anisotropic distortion of cages. Specifically, the compression of cages along the x and z directions is accommodated by an elongation along the y axis, resulting in an overall framework expansion along this direction. In X-dia-2-Cd, NLC is also confirmed by the pressure-dependent lattice evolution. As shown in Fig. S7–S10 and Table S8, upon contraction from the Lp to Np phase, the supercell volume decreases and the x and z axes contract, while the y axis exhibits anomalous elongation. This phenomenon is consistent with experimental observations on MIL-53(Al) and MIL-53-NH_2(Al).[64] These results indicate that in X-dia-2-Cd, following the structural transition, compliance along the y axis remains essentially unchanged, while the softening along the x and z axes reflects that 1D channels expand predominantly along these directions.

Young's modulus (E) reflects the reversible stiffness response to elastic deformation along a crystallographic axis. Fig. 7a and b show 3D surfaces of E of CO_2-loaded X-dia-2-Cd at 273 K,

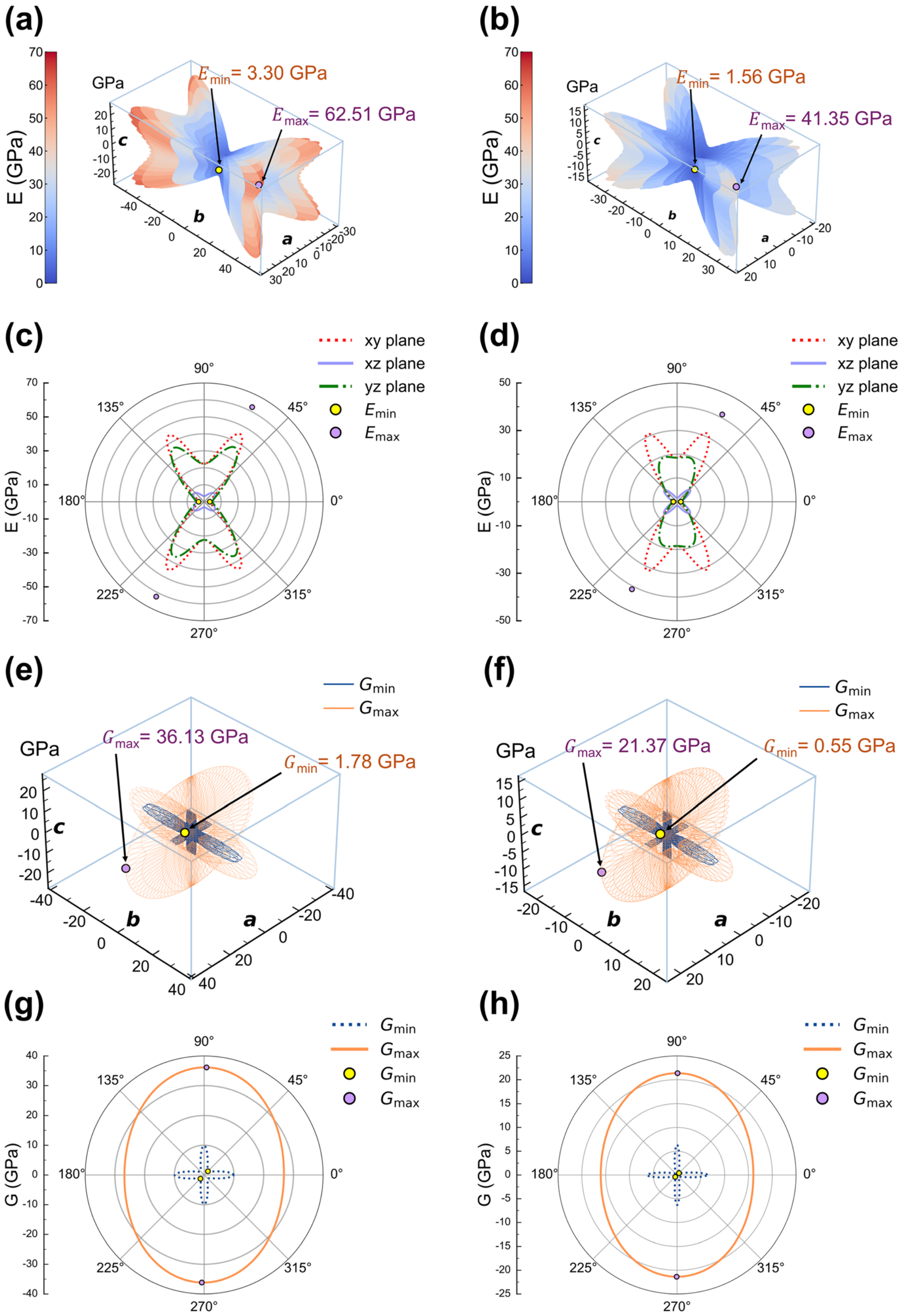

Fig. 7 Anisotropic 3D surfaces of Young's moduli (E) of CO_2-loaded X-dia-2-Cd at 273 K: (a) 2.5 bar in the Np phase and (b) 30 bar in the Lp phase. Polar plots of 3D surfaces of E obtained *via* projection onto three orthonormal planes at 273 K: (c) 2.5 bar in the Np phase and (d) 30 bar in the Lp phase. Anisotropic 3D surfaces of shear moduli (G) of CO_2-loaded X-dia-2-Cd at 273 K: (e) 2.5 bar in the Np phase and (f) 30 bar in the Lp phase. The orange and blue color coding denotes the maximum and minimum moduli, respectively, at each point (θ, ϕ, χ) point of 3D spherical coordinates.[56] Polar plots of 3D surfaces of G obtained *via* projection onto three orthonormal planes at 273 K (g) 2.5 bar in the Np phase and (h) 30 bar in the Lp phase.

Table 1 Elastic properties of CO_2-loaded X-dia-2-Cd at 195 K and 273 K

Elastic properties	Np phase, 195 K	Lp phase, 195 K	Np phase, 273 K	Lp phase, 273 K
Bulk modulus, K (GPa)[a]	12.57	11.49	12.00	10.11
Young's modulus, E (GPa)[a]	26.87	19.19	24.79	15.67
Shear modulus, G (GPa)[a]	11.75	7.85	10.77	6.31
A_E[b]	17.86	20.34	18.98	28.73
A_G[b]	19.78	26.61	20.71	42.78

[a] K, E and G were evaluated using the Hill scheme. [b] The anisotropy index A is defined as the ratio of maximum to minimum E or G.

highlighting the pronounced anisotropy in both Np and Lp phases. In the Np phase, E ranges from 3.30 to 62.51 GPa, whereas in the Lp phase, the range decreases between 1.56 and 41.35 GPa, indicating a general softening upon transition from the Np to Lp phase. The corresponding 2D projections on the xy, yz, and xz planes (Fig. 7c and d) reveal that the minimum of E ($E_{\min}$) consistently occurs at the intersection of the xy plane and the x axis, while the maximum of E ($E_{\max}$) lies outside these planes. Such an observation suggests that the most compliant direction is along the [100] crystallographic axis, whereas the stiffest direction is oriented off the principal plane, aligned with the orientation of continuous Cd-HImbz-Cd connectivity (Fig. S20a).

Shear modulus (G) represents the resistance to shape change under shear stress, reflecting the directional rigidity along an angular distortion. Fig. 7e and f illustrate 3D surfaces of G of CO_2-loaded X-dia-2-Cd at 273 K. In the Np phase, the minimum G ($G_{\min}$) reaches 1.78 GPa, while the maximum G ($G_{\max}$) attains 36.13 GPa. In the Lp phase, these extrema decrease to 0.55 and 21.37 GPa, respectively, indicating a pronounced reduction in shear rigidity after framework expansion. The corresponding 2D projections on the xz plane (Fig. 7g and h) further indicate that the lowest shear resistance is oriented along the diagonal direction between the x and z axes, whereas the direction associated with higher shear resistance is aligned with the x axis. From a structural perspective, the origin of a low shear resistance ($G_{\min}$) can be rationalized by the rectangular cross-section of 1D channels, which is inherently vulnerable to a shear deformation. This behavior arises from the compliant Cd metal nodes located at the four corners of the channel, while the HImbz linkers act as comparatively rigid bridging units (Fig. S20b). As a result, the framework connectivity closely resembles a pin-jointed truss, a mechanical motif that is intrinsically unstable under shear loading. Similarly, low $G_{\min}$ was also observed in the wine-rack MOF MIL-53,[65] which exhibits comparable mechanical behavior, underscoring the intrinsically high elastic anisotropy common in flexible MOFs.

As summarized in Table 1, E and G of CO_2-loaded X-dia-2-Cd exhibit strong directional variations, reflecting a highly anisotropic mechanical response in both Np and Lp phases. Upon structural transition, the framework undergoes a general softening in both E and G, decreasing from 26.87 and 11.75 GPa to 19.19 and 7.85 GPa at 195 K, respectively. This trend of softening becomes even more pronounced at 273 K, where E drops sharply from 24.79 to 15.67 GPa and G drops from 10.77 to 6.31 GPa. Concurrently, the structural expansion severely amplifies the mechanical anisotropy of the elastic response, as evidenced by the increased A_E and A_G values. Specifically, at 195 K, A_E and A_G increase from 17.86 and 19.78 in the Np phase to 20.34 and 26.61 in the Lp phase, respectively. This anisotropic amplification is particularly striking at 273 K, where A_E and A_G further escalate to 28.73 and 42.78, indicating that the expanded Lp phase possesses extreme mechanical heterogeneity. This is essentially attributed to the weakening of load-bearing metal-linker interactions and the enhancement of structural compliance during framework expansion. The elastic results discussed above, including the quantitative Voigt, Reuss and Hill averages of K, E and G, together with the corresponding extrema of anisotropic elastic moduli derived from the Hill scheme, are listed in Tables S9–S12.

4 Conclusions

Through hybrid GCMC/MD simulations, we accurately capture the framework flexibility of X-dia-2-Cd. The relaxed structure is consistent with DFT-optimized and experimental structures. During structural transition from the Np to Lp phase, stepped CO_2 adsorption isotherms at 195 K and 273 K are correctly predicted, in line with experimental observations. The structural transition is attributed to the deformation of Cd metal nodes and the widening of adamantoid cages, as reflected by the changes in the angles of Cd metal nodes, and further causes the expansion of 1D channels. Upon structural transition, CO_2 molecules diffuse markedly faster in the Lp phase than in the Np phase. From the radial distribution functions between CO_2 molecules and framework atoms, we reveal the distinct interactions of CO_2 molecules in Np and Lp phases at the molecular level, providing microscopic insights into their unique adsorption behavior. Moreover, we explore the relationships between the mechanical properties of X-dia-2-Cd and its inherent flexibility. Upon structural transition, the intrinsic bulk modulus reduces, whereas CO_2 adsorption mitigates this softening. Notably, anomalous negative linear compressibility exists along the y axis. The framework exhibits anisotropic elastic properties, and the origin of directionally dependent mechanical behavior is fundamentally elucidated. We anticipate that the hybrid simulation protocol adopted in this study can be extended to a wide temperature range for the adsorption of CO_2 and other adsorbates, facilitating the rational design of nextgeneration MOFs for high-performance gas storage and separation.

Author contributions

R. Z. conceived the work, carried out all the simulations, and wrote the manuscript. S. A. M. provided technical guidance for the calculation of mechanical properties. Q. L. assisted with the selection of force fields. X. W. provided supervision, advised on simulation strategies and approaches, and participated in manuscript writing. J. J. conceptualized the project, contributed to manuscript writing and editing, acquired the funding and supervised the project. All authors participated in the discussion and reviewed the manuscript.

Conflicts of interest

The authors declare no competing financial interest.

Data availability

Data supporting this work have been provided in the supplementary information (SI). Supplementary information: force field parameters, force field validation, convergence of hybrid GCMC/MD simulations, validation of mechanical property calculations, structure optimization, CO_2 adsorption in X-dia-2-Cd, and mechanical properties of X-dia-2-Cd. See DOI: https://doi.org/10.1039/d6ta01626j.

Acknowledgements

We gratefully acknowledge the National Research Foundation Singapore (NRF-CRP26-2021RS-0002) and A*STAR LCER-FI projects (LCERFI01-0015 U2102d2004 and LCERFI01-0033 U2102d2006) for financial support, and the National University of Singapore (CFP01-CF-077 and CFP03-CF-016) and National Supercomputing Centre (NSCC) Singapore for computational resources.

References

1 K. V. Kumar, K. Preuss, M.-M. Titirici and F. Rodríguez-Reinoso, Nanoporous Materials for the Onboard Storage of Natural Gas, *Chem. Rev.*, 2017, **117**, 1796–1825.
2 Z. Chen, K. O. Kirlikovali, K. B. Idrees, M. C. Wasson and O. K. Farha, Porous materials for hydrogen storage, *Chem*, 2022, **8**, 693–716.
3 R. E. Morris and P. S. Wheatley, Gas Storage in Nanoporous Materials, *Angew. Chem., Int. Ed.*, 2008, **47**, 4966–4981.
4 F. Deng, Z. Chen, C. Wang, C. Xiang, P. Poredoš and R. Wang, Hygroscopic Porous Polymer for Sorption-Based Atmospheric Water Harvesting, *Adv. Sci.*, 2022, **9**, 2204724.
5 W. Song, Z. Zheng, A. H. Alawadhi and O. M. Yaghi, MOF water harvester produces water from Death Valley desert air in ambient sunlight, *Nat. Water*, 2023, **1**, 626–634.
6 D. Alezi, Y. Belmabkhout, M. Suyetin, P. M. Bhatt, Ł. J. Weseliński, V. Solovyeva, K. Adil, I. Spanopoulos, P. N. Trikalitis, A.-H. Emwas and M. Eddaoudi, MOF Crystal Chemistry Paving the Way to Gas Storage Needs: Aluminum-Based soc-MOF for CH_4, O_2 and CO_2 Storage, *J. Am. Chem. Soc.*, 2015, **137**, 13308–13318.
7 J. M. Huck, L.-C. Lin, A. H. Berger, M. N. Shahrak, R. L. Martin, A. S. Bhown, M. Haranczyk, K. Reuter and B. Smit, Evaluating different classes of porous materials for carbon capture, *Energy Environ. Sci.*, 2014, **7**, 4132–4146.
8 G. Singh, J. Lee, A. Karakoti, R. Bahadur, J. Yi, D. Zhao, K. AlBahily and A. Vinu, Emerging trends in porous materials for CO_2 capture and conversion, *Chem. Soc. Rev.*, 2020, **49**, 4360–4404.
9 J. Liu, P. K. Thallapally, B. P. McGrail, D. R. Brown and J. Liu, Progress in adsorption-based CO_2 capture by metal–organic frameworks, *Chem. Soc. Rev.*, 2012, **41**, 2308–2322.
10 K. Sumida, D. L. Rogow, J. A. Mason, T. M. McDonald, E. D. Bloch, Z. R. Herm, T.-H. Bae and J. R. Long, Carbon Dioxide Capture in Metal–Organic Frameworks, *Chem. Rev.*, 2012, **112**, 724–781.
11 T. A. Makal, J.-R. Li, W. Lu and H.-C. Zhou, Methane storage in advanced porous materials, *Chem. Soc. Rev.*, 2012, **41**, 7761–7779.
12 A. Subanbekova, V. I. Nikolayenko, A. A. Bezrukov, D. Sensharma, N. Kumar, D. J. O'Hearn, V. Bon, S.-Q. Wang, K. Koupepidou, S. Darwish, S. Kaskel and M. J. Zaworotko, Water vapour and gas induced phase transformations in an 8-fold interpenetrated diamondoid metal-organic framework, *J. Mater. Chem. A*, 2023, **11**, 9691–9699.
13 E. J. Carrington, C. A. McAnally, A. J. Fletcher, S. P. Thompson, M. Warren and L. Brammer, Solvent-switchable continuous-breathing behaviour in a diamondoid metal–organic framework and its influence on CO_2 versus CH_4 selectivity, *Nat. Chem.*, 2017, **9**, 882–889.
14 Q.-Y. Yang, P. Lama, S. Sen, M. Lusi, K.-J. Chen, W.-Y. Gao, M. Shivanna, T. Pham, N. Hosono, S. Kusaka, J. J. Perry IV, S. Ma, B. Space, L. J. Barbour, S. Kitagawa and M. J. Zaworotko, Reversible Switching between Highly Porous and Nonporous Phases of an Interpenetrated Diamondoid Coordination Network That Exhibits Gate-Opening at Methane Storage Pressures, *Angew. Chem., Int. Ed.*, 2018, **57**, 5684–5689.
15 K. Roztocki, F. Formalik, A. Krawczuk, I. Senkovska, B. Kuchta, S. Kaskel and D. Matoga, Collective Breathing in an Eightfold Interpenetrated Metal–Organic Framework: From Mechanistic Understanding towards Threshold Sensing Architectures, *Angew. Chem., Int. Ed.*, 2020, **59**, 4491–4497.
16 S.-M. Wang, M. Shivanna, P. Lama, Q.-Y. Yang, L. J. Barbour and M. J. Zaworotko, Metal Doping to Control Gate Opening and Increase Methane Working Capacity in Isostructural Flexible Diamondoid Networks, *ChemSusChem*, 2023, **16**, e202300069.
17 A. U. Ortiz, A. Boutin, A. H. Fuchs and F.-X. Coudert, Investigating the Pressure-Induced Amorphization of Zeolitic Imidazolate Framework ZIF-8: Mechanical

Instability Due to Shear Mode Softening, *J. Phys. Chem. Lett.*, 2013, **4**, 1861–1865.

18 A. V. Neimark, F.-X. Coudert, C. Triguero, A. Boutin, A. H. Fuchs, I. Beurroies and R. Denoyel, Structural Transitions in MIL-53(Cr): View from Outside and Inside, *Langmuir*, 2011, **27**, 4734–4741.

19 Q. Ma, Q. Yang, A. Ghoufi, G. Férey, C. Zhong and G. Maurin, Guest dependent pressure behavior of the flexible MIL-53(Cr): A computational exploration, *Dalton Trans.*, 2012, **41**, 3915–3919.

20 F.-X. Coudert, A. Boutin, A. H. Fuchs and A. V. Neimark, Adsorption Deformation and Structural Transitions in Metal–Organic Frameworks: From the Unit Cell to the Crystal, *J. Phys. Chem. Lett.*, 2013, **4**, 3198–3205.

21 T. Kundu, B. B. Shah, L. Bolinois and D. Zhao, Functionalization-Induced Breathing Control in Metal–Organic Frameworks for Methane Storage with High Deliverable Capacity, *Chem. Mater.*, 2019, **31**, 2842–2847.

22 A. Ghoufi, A. Subercaze, Q. Ma, P. G. Yot, Y. Ke, I. Puente-Orench, T. Devic, V. Guillerm, C. Zhong, C. Serre, G. Férey and G. Maurin, Comparative Guest, Thermal, and Mechanical Breathing of the Porous Metal Organic Framework MIL-53(Cr): A Computational Exploration Supported by Experiments, *J. Phys. Chem. C*, 2012, **116**, 13289–13295.

23 M. Agrawal and D. S. Sholl, Effects of Intrinsic Flexibility on Adsorption Properties of Metal–Organic Frameworks at Dilute and Nondilute Loadings, *ACS Appl. Mater. Interfaces*, 2019, **11**, 31060–31068.

24 S. M. J. Rogge, R. Goeminne, R. Demuynck, J. J. Gutiérrez-Sevillano, S. Vandenbrande, L. Vanduyfhuys, M. Waroquier, T. Verstraelen and V. Van Speybroeck, Modeling Gas Adsorption in Flexible Metal–Organic Frameworks via Hybrid Monte Carlo/Molecular Dynamics Schemes, *Adv. Theory Simul.*, 2019, **2**, 1800177.

25 L. Zhang, Z. Hu and J. Jiang, Sorption-Induced Structural Transition of Zeolitic Imidazolate Framework-8: A Hybrid Molecular Simulation Study, *J. Am. Chem. Soc.*, 2013, **135**, 3722–3728.

26 K. Zhang, L. Zhang and J. Jiang, Adsorption of C_1–C_4 Alcohols in Zeolitic Imidazolate Framework-8: Effects of Force Fields, Atomic Charges, and Framework Flexibility, *J. Phys. Chem. C*, 2013, **117**, 25628–25635.

27 Z. Yu, D. M. Anstine, S. E. Boulfelfel, C. Gu, C. M. Colina and D. S. Sholl, Incorporating Flexibility Effects into Metal–Organic Framework Adsorption Simulations Using Different Models, *ACS Appl. Mater. Interfaces*, 2021, **13**, 61305–61315.

28 S. A. Mohamed, R. Zheng, N. Zhu, D. Zhao and J. Jiang, A Systematic Approach for Incorporating Structural Flexibility in High-Throughput Computational Screening of Metal–Organic Frameworks for Xylene Separation, *J. Am. Chem. Soc.*, 2025, **147**, 12251–12262.

29 R. Zheng, X. Wu, S. A. Mohamed and J. Jiang, Unraveling Guest-Induced Structural Transition in a Flexible Metal–Organic Framework for C_4 Alkane/Alkene Separation, *Chem. Mater.*, 2025, **37**, 4807–4817.

30 S. Bureekaew, S. Amirjalayer, M. Tafipolsky, C. Spickermann, T. K. Roy and R. Schmid, MOF-FF – A Flexible First-Principles Derived Force Field for Metal-Organic Frameworks, *Phys. Status Solidi B*, 2013, **250**, 1128–1141.

31 A. K. Rappe, C. J. Casewit, K. S. Colwell, W. A. I. Goddard and W. M. Skiff, UFF, A Full Periodic Table Force Field for Molecular Mechanics and Molecular Dynamics Simulations, *J. Am. Chem. Soc.*, 1992, **114**, 10024–10035.

32 M. A. Addicoat, N. Vankova, I. F. Akter and T. Heine, Extension of the Universal Force Field to Metal–Organic Frameworks, *J. Chem. Theory Comput.*, 2014, **10**, 880–891.

33 D. E. Coupry, M. A. Addicoat and T. Heine, Extension of the Universal Force Field for Metal–Organic Frameworks, *J. Chem. Theory Comput.*, 2016, **12**, 5215–5225.

34 A. V. Neimark, F.-X. Coudert, A. Boutin and A. H. Fuchs, Stress-Based Model for the Breathing of Metal–Organic Frameworks, *J. Phys. Chem. Lett.*, 2010, **1**, 445–449.

35 J. J. Potoff and J. I. Siepmann, Vapor–liquid equilibria of mixtures containing alkanes, carbon dioxide, and nitrogen, *AICHE J.*, 2001, **47**, 1676–1682.

36 S. Kancharlapalli, A. Gopalan, M. Haranczyk and R. Q. Snurr, Fast and Accurate Machine Learning Strategy for Calculating Partial Atomic Charges in Metal−Organic Frameworks, *J. Chem. Theory Comput.*, 2021, **17**, 3052–3064.

37 G. Zhao and Y. G. Chung, PACMAN: A Robust Partial Atomic Charge Predicter for Nanoporous Materials Based on Crystal Graph Convolution Networks, *J. Chem. Theory Comput.*, 2024, **20**, 5368–5380.

38 J. Luo, O. B. Said, P. Xie, M. Gibaldi, J. Burner, C. Pereira and T. K. Woo, MEPO-ML: a robust graph attention network model for rapid generation of partial atomic charges in metal-organic frameworks, *npj Comput. Mater.*, 2024, **10**, 224.

39 P. G. Boyd, S. M. Moosavi, M. Witman and B. Smit, Force-Field Prediction of Materials Properties in Metal-Organic Frameworks, *J. Phys. Chem. Lett.*, 2017, **8**, 357–363.

40 S. L. Mayo, B. D. Olafson and W. A. Goddard, DREIDING: a generic force field for molecular simulations, *J. Phys. Chem. C*, 1990, **94**, 8897–8909.

41 A. P. Thompson, H. M. Aktulga, R. Berger, D. S. Bolintineanu, W. M. Brown, P. S. Crozier, P. J. in 't Veld, A. Kohlmeyer, S. G. Moore, T. D. Nguyen, R. Shan, M. J. Stevens, J. Tranchida, C. Trott and S. J. Plimpton, LAMMPS - A flexible simulation tool for particle-based materials modeling at the atomic, meso, and continuum scales, *Comput. Phys. Commun.*, 2022, **271**, 108171.

42 T. D. Kühne, M. Iannuzzi, M. Del Ben, V. V. Rybkin, P. Seewald, F. Stein, T. Laino, R. Z. Khaliullin, O. Schütt, F. Schiffmann, D. Golze, J. Wilhelm, S. Chulkov, M. H. Bani-Hashemian, V. Weber, U. Borštnik, M. Taillefumier, A. S. Jakobovits, A. Lazzaro, H. Pabst, T. Müller, R. Schade, M. Guidon, S. Andermatt, N. Holmberg, G. K. Schenter, A. Hehn, A. Bussy, F. Belleflamme, G. Tabacchi, A. Glöß, M. Lass, I. Bethune, C. J. Mundy, C. Plessl, M. Watkins, J. VandeVondele, M. Krack and J. Hutter, CP2K: An electronic structure and molecular dynamics software package - Quickstep: Efficient

and accurate electronic structure calculations, *J. Chem. Phys.*, 2020, **152**, 194103.

43 A. Gelman and D. B. Rubin, Inference from Iterative Simulation Using Multiple Sequences, *Stat. Sci.*, 1992, **7**, 457–472.

44 A. Vehtari, A. Gelman, D. Simpson, B. Carpenter and P.-C. Bürkner, Rank-normalization, folding, and localization: An improved $\hat{R}$ for assessing convergence of MCMC (with discussion), *Bayesian Anal.*, 2021, **16**, 667–718.

45 D. M. Anstine, A. G. Demidov, N. F. Mendez, W. J. Morgan and C. M. Colina, Screening PIM-1 performance as a membrane for binary mixture separation of gaseous organic compounds, *J. Membr. Sci.*, 2020, **599**, 117798.

46 D. M. Anstine, N. F. Mendez and C. M. Colina, Sulfonyl PIM-1: A diverse separation membrane with dilation resistance, *AICHE J.*, 2021, **67**, e17006.

47 D. M. Anstine, D. Tang, D. S. Sholl and C. M. Colina, Adsorption space for microporous polymers with diverse adsorbate species, *npj Comput. Mater.*, 2021, **7**, 53.

48 K. B. Idrees, Z. Li, H. Xie, K. O. Kirlikovali, M. Kazem-Rostami, X. Wang, X. Wang, T. Y. Tai, T. Islamoglu, J. F. Stoddart, R. Q. Snurr and O. K. Farha, Separation of Aromatic Hydrocarbons in Porous Materials, *J. Am. Chem. Soc.*, 2022, **144**, 12212–12218.

49 D. Dubbeldam, S. Calero, D. E. Ellis and R. Q. Snurr, RASPA: molecular simulation software for adsorption and diffusion in flexible nanoporous materials, *Mol. Simul.*, 2016, **42**, 81–101.

50 C. Gu, Z. Yu, J. Liu and D. S. Sholl, Construction of an Anion-Pillared MOF Database and the Screening of MOFs Suitable for Xe/Kr Separation, *ACS Appl. Mater. Interfaces*, 2021, **13**, 11039–11049.

51 S. H. Jamali, L. Wolff, T. M. Becker, M. de Groen, M. Ramdin, R. Hartkamp, A. Bardow, T. J. H. Vlugt and O. A. Moultos, OCTP: A Tool for On-the-Fly Calculation of Transport Properties of Fluids with the Order-n Algorithm in LAMMPS, *J. Chem. Inf. Model.*, 2019, **59**, 1290–1294.

52 S. A. Mohamed, D. Zhao and J. Jiang, Integrating stability metrics with high-throughput computational screening of metal–organic frameworks for CO_2 capture, *Commun. Mater.*, 2023, **4**, 79.

53 X. Wu, Q. Liu and J. Jiang, Discovering robust metal—organic frameworks with open copper sites for precombustion CO_2 capture: Data-efficient exploration and exploitation by active learning, *Chem. Eng. J.*, 2025, **521**, 167021.

54 M. Parrinello and A. Rahman, Strain fluctuations and elastic constants, *J. Chem. Phys.*, 1982, **76**, 2662–2666.

55 N. Castel and F.-X. Coudert, Computation of Finite Temperature Mechanical Properties of Zeolitic Imidazolate Framework Glasses by Molecular Dynamics, *Chem. Mater.*, 2023, **35**, 4038–4047.

56 R. Gaillac, P. Pullumbi and F.-X. Coudert, ELATE: an open-source online application for analysis and visualization of elastic tensors, *J. Phys.:Condens. Matter*, 2016, **28**, 275201.

57 Y. Cho, J. Teetz and H. J. Kulik, Assessing UFF and DFT-Tuned Force Fields for Predicting Experimental Isotherms of MOFs, *J. Chem. Inf. Model.*, 2025, **65**, 3451–3460.

58 B. Wang, J. Ke, X. Chen, Y. Sun, P. Ren and J. Zhang, Anomalous Loading Rate Dependence of the Mechanical Properties of Metal–Organic Framework Crystals: Latent Heat Effects of the Pressure-Induced Local Phase Transition, *J. Phys. Chem. Lett.*, 2023, **14**, 9464–9471.

59 B. Wang, J. Ke and J. Zhang, Thermomechanical properties of metal–organic framework HKUST-1 crystals, *J. Mater. Chem. A*, 2024, **12**, 15071–15081.

60 R. S. Haines and R. McIntosh, Length Changes of Activated Carbon Rods Caused by Adsorption of Vapors, *J. Chem. Phys.*, 1947, **15**, 28–38.

61 F. Mouhat, D. Bousquet, A. Boutin, L. Bouëssel du Bourg, F.-X. Coudert and A. H. Fuchs, Softening upon Adsorption in Microporous Materials: A Counterintuitive Mechanical Response, *J. Phys. Chem. Lett.*, 2015, **6**, 4265–4269.

62 S. Parashar, N. J. Corrente and A. V. Neimark, Unveiling non-monotonic deformation of flexible MOFs during gas adsorption: From contraction and softening to expansion and hardening, *J. Colloid Interface Sci.*, 2025, **686**, 88–95.

63 A. Emelianova, C. Balzer, G. Reichenauer and G. Y. Gor, Adsorption-Induced Deformation of Zeolites 4A and 13X: Experimental and Molecular Simulation Study, *Langmuir*, 2023, **39**, 11388–11397.

64 P. Serra-Crespo, A. Dikhtiarenko, E. Stavitski, J. Juan-Alcañiz, F. Kapteijn, F.-X. Coudert and J. Gascon, Experimental evidence of negative linear compressibility in the MIL-53 metal–organic framework family, *CrystEngComm*, 2015, **17**, 276–280.

65 A. U. Ortiz, A. Boutin, A. H. Fuchs and F.-X. Coudert, Anisotropic Elastic Properties of Flexible Metal-Organic Frameworks: How Soft are Soft Porous Crystals?, *Phys. Rev. Lett.*, 2012, **109**, 195502.